Simulation of induced seismic ground motions using coupled geomechanical and seismic wave propagation models

Bob Paap [1,2] Dirk Kraaijpoel,[1] Brecht Wassing[1] and Jan-Diederik van Wees[1,2]

[1]*TNO, Applied Geosciences, Utrecht, The Netherlands. E-mail: bob.paap@tno.nl*
[2]*, Utrecht University, Department of Earth Sciences, Tectonics, Utrecht, The Netherlands,*

SUMMARY

Numerical simulations of seismic wave propagation usually rely on a simple source model consisting of an idealized point location and a moment tensor. In general, this is a valid approximation when the source dimensions are small relative to the distance of points at which the seismic wave motions are to be evaluated. Otherwise, a more realistic spatio-temporal source representation is required to accurately calculate ground motions at the position of monitoring stations. Here, we present a generic approach to couple geomechanical simulations to seismic wave propagation models using the concept of the equivalent force field. This approach allows the simulation of seismic wave propagation resulting from the spatio-temporal dependent earthquake nucleation and rupture processes. Within the geomechanical package two separate geomechanics codes are used to simulate both the slow loading stage leading to earthquake nucleation as well as the successive dynamic rupture stage. We demonstrate the approach to a case of induced seismicity, where fault reactivation occurs due to production from a natural gas reservoir.

Key words: Numerical modelling; Computational seismology; Induced seismicity; Wave propagation.

1 INTRODUCTION

Earthquake simulations are commonly conducted to calculate synthetic surface recordings to evaluate observed surface recordings. With increasing distance between the earthquake's location and distant monitoring stations, spatio-temporal aspects of the source mechanism can be neglected, where it can be approximated by an instantaneous event that occurs at a single point in space and time. Consideration of rupture dynamics for far-field ground motion simulations becomes increasingly relevant for smaller source-station distances, especially for induced earthquakes related to energy production and storage in the upper few kilometres of the subsurface.

During energy production and storage operations, the respective extraction or injection of fluids cause changes in pore pressure and related stress perturbations in the reservoir host rock. Locally, the stress perturbations may cause fault (re)activation and stress release through seismic rupture events (earthquakes). The induced seismic vibrations that propagate away from the source may, on the one hand, result in ground motions at the surface that are strong enough to cause nuisance or even damage. Ultimately, these ground motions may pose a safety threat to the local population. On the other hand, the ground motions may carry information on the reservoir state and processes that is otherwise hard to obtain due to lack of direct *in situ* measurements. A good understanding of the seismic vibrations and their relationship to the subsurface processes that cause them

is therefore beneficial in two ways: first, for induced seismic hazard and risk assessment, and second, for the seismic characterization of subsurface processes.

Evolution of reservoir pore pressures due to fluid injection or extraction and the effect on the stress and strain in the reservoir rock can be modeled using quasi-static geomechanical models (Nagelhout & Roest 1997; Mulders 2003; Orlic & Wassing 2013). These models are quasi-static in the sense that the relevant time scales are sufficiently long that at each instance of time the reservoir state can be approximated by mechanical equilibrium. This approximation no longer holds when the stress level in the host rock locally starts to exceed the shear strength of the faults and fractures. Depending on the rock properties, an instability may escalate over short timescales, leading to rupture and large-magnitude particle motion. Dynamic rupture simulations rely on the dynamic equations of motions and are used to provide insight in the mechanisms of fault stress evolution and the timing and mode of fault reactivation (Cappa & Rutqvist 2012; Zbinden *et al.* 2017; Buijze *et al.* 2019).

In principle, geomechanical modelling codes that simulate dynamic fault rupture and resulting motions in the near-source region, are also capable of simulating the seismic wave propagation away from the source area and into the far-field and the surface. However, calculation of far-field surface ground motions at the spatial scales of regular monitoring networks can be a computational challenge

with dynamic rupture modelling. In practice, seismic wave propagation simulations are performed using dedicated seismic wave propagation codes that make use of numerically efficient assumptions, such as small strains and linear constitutive equations. As a result, these codes have a higher efficiency on the typical associated spatial scales, that is in propagation over tens to hundreds of wavelengths in distance.

Seismic wave propagation codes generally adopt point-source representations, which is a simplification of the actual rupture mechanism that occurs along a fault plane, that is a time- and space-dependent volume or surface source. A point-source representation can be sufficiently accurate, when dimensions of the rupture zone are small compared to the source-station distances. However, the point source representation becomes less accurate when simulating rupture mechanisms of moderate earthquakes in the shallow subsurface. In that case, the rupture process would be preferably calculated by a dynamic rupture simulation while still efficiently calculating far-field ground motions, which requires a coupling between geomechanic and seismic wave propagation codes.

Wang & Cai (2016) demonstrate an approach to couple the geomechanical FLAC3D (Fast Lagrangian analysis of continua) package to the wave propagation package SPECFEM2D, with the objective to determine a non-uniform velocity field for excavated underground mines based on a nonlinear relation between confining stress and wave velocity. Using a coupled FLAC/SPECFEM2D modelling approach, they simulate ground motions around a stope due to a fault-slip seismic event. In their study, they prescribe a point source model in SPECFEM2D which are regularly used to represent mining-induced seismic events. Kaneko *et al.* (2011) developed a spectral element method to model the processes of slow loading and dynamic rupture. This enables them to simulate all stages of the earthquake cycle, that is the nucleation process, the dynamic rupture propagation and the post-seismic slip and aseismic slip throughout the tectonic loading period. Buijze *et al.* (2019) conducted dynamic simulations of fault reactivation and seismic rupture induced by reservoir depletion for the Groningen gas field.

Here, we present a generic approach to couple any geomechanics code capable of dynamic rupture simulation to a seismic wave propagation code. The purpose is to be able to take advantage of the complete physics available in the geomechanics code, while also taking advantage of the efficiency of dedicated seismic wave propagation code. We demonstrate the approach in the context of induced seismicity due to gas production from a natural gas reservoir. We identify three modelling stages.

The first stage involves the relatively slow geomechanical evolution of a reservoir from its initial, 'virgin' state under the influence of ongoing pore pressure depletion and is calculated with a geomechanics code. The evolution of the stress-state on any pre-existing fault towards the start of the rupture depends on the pore pressure changes, poro-elastic effects and reservoir compaction, but also on the particular fault and reservoir geometries. In the second stage fault reactivation and dynamic rupture are simulated with a second geomechanics code. In the third stage, the resulting seismic wave propagation towards the far-field is calculated on a larger spatial scale. This is done by translating the displacement field calculated in the second dynamic rupture stage to an equivalent force field using the equation of motion. Next, this equivalent force field is released in a seismic modelling package to calculate elastic wave propagation to the surface. This approach has an additional advantage that in the third stage the propagating wavefield that results from the release of the equivalent force field, can freely interact with reflectors both inside and outside the source region, even if the

reflectors are not present in the geomechanical model from stage 1 and 2.

2 MODEL DESCRIPTION FOR CASE OF DEPLETING GAS FIELD

To make the application of the coupled modelling approach more specific we consider a setting analogue to the Groningen gas production site, where earthquakes are induced by reactivation of pre-existing faults resulting from reservoir compaction due to gas production (van Thienen-Visser & Breunesse 2015).

2.1 Numerical modelling packages

We implement and evaluate the coupled modelling approach using FLAC3D and SPECFEM2D, both being used before specifically for studies on producing gas fields like the Groningen gas field (Wassing *et al.* 2017; Paap *et al.* 2018). Both packages are state-of-the-art simulators in their own fields of expertise. Though FLAC3D is tailored to perform numerical simulations for arbitrary 3-D models, we here chose a model set up with an out-of-plane thickness of one cell and fixed boundary conditions, representative of plane-strain conditions. In this paper we refer to the FLAC3D software as FLAC. For SPECFEM both a 2-D and 3-D version are available. We refer to SPECFEM2D used in this study as SPECFEM in the remainder of this paper.

Several differences exist between FLAC and SPECFEM. FLAC is a finite difference program that uses a Lagrangian analysis (Itasca 2013), whereas SPECFEM uses the spectral element method (Komatitsch & Tromp 1999). FLAC enables non-linear material behaviour allowing large strains and implementing the full dynamic equation of motion, whereas SPECFEM assumes linear material behaviour restricted to small strains and implements the weak form of the equation of motion. In FLAC, linear simulations run slower compared to equivalent finite element programs and is most effective for non-linear behaviour (such as rupture) or large strain problems (Itasca 2013).

FLAC is a commercial, finite difference software code that can simulate a wide range of nonlinear static and dynamic geomechanical problems. The software of FLAC can be used to simulate the complex behaviour of fault systems under changing stress fields, such as the simulation of stress changes for CO_2 storage (Rutqvist *et al.* 2011) and for enhanced geothermal systems (Wassing *et al.* 2014) or in a depleting gas reservoir (Wassing *et al.* 2016, 2017; Zbinden *et al.* 2017). FLAC can be run in either quasi-static mode, for example for simulation of slowly evolving stress conditions during long-term reservoir depletion, or dynamic mode, for simulation of fast rupture processes on critically stressed faults. This package covers a wide range of physical conditions, including large (finite) strains and non-linear constitutive relations. For both static and dynamic analyses, an explicit, dynamic solution scheme is used to solve the full dynamic equations of motion. For (quasi-)static problems, apparent mass and inertia terms are used to reach the equilibrium state in a numerically stable manner. For dynamic problems, gridpoint masses derived from real densities are used to solve the full equations of motion (Itasca 2013).

Benchmark tests between FLAC and wave propagation models have demonstrated the capability of using FLAC for wave propagation modelling (Itasca 2013). However, for linear material behaviour FLAC is not as efficient as other dedicated modelling tools (Itasca 2013), because the calculations for nonlinear terms still take place

when they are not really required. Several numerical techniques are available for linear wave propagation simulations, such as the finite difference method (Kelly *et al.* 1976; Levander 1988), the pseudo spectral method (PSM) (Kosloff & Baysal 1982; Klin *et al.* 2010), the finite element method (FEM) (Bao *et al.* 1998; Bielak *et al.* 2003), and the spectral element method (SEM) (Patera 1984; Komatitsch & Tromp 1999; Tromp *et al.* 2008). These techniques each have trade-offs in numerical dispersion, spurious waves and computation cost. The SEM technique is a specific version of FEM, where the so-called spectral elements aim at diagonalizing the mass matrix calculations, making it particularly suited for linear hyperbolic partial differential equations, such as wave propagation. Because the mass matrix is diagonal, no linear system needs to be inverted, which makes it favorable to implement on parallel systems (Komatitsch & Tromp 1999). With that it has accuracy comparable to the PSM with the model discretization flexibility of the FEM. Compared to FEM, SEM uses a high-order basis function that makes the method accurate enough to solve the wave equation with four to five nodes per wavelength (Komatitsch & Tromp 1999). SPECFEM software uses the SEM technique and is a powerful tool for acoustic, (an)elastic, and poroelastic seismic wave propagation modelling, and allows linear material behaviour as applicable to relatively small strains. It is particularly well-suited for handling complex geometries and interface conditions and has good accuracy and convergence properties (Maday & Patera 1989; Cohen 2002; Seriani & Oliveira 2008). It is designed to be implemented parallel on very large supercomputers and on GPU clusters (Komatitsch *et al.* 2008; Komatitsch 2011; Tsuboi *et al.* 2016).

2.2 Geomechanical model description of depleting gas field

We consider a model based on a simplified geometry of the producing gas reservoir in Groningen, which is an extensional tectonic setting. The model is intersected by a single fault with a dip of 70° and 100 m offset (van Wees *et al.* 2018). The reservoir is surrounded by caprock, over- and underburden. The simulation includes pressure depletion, reservoir compaction and the associated poroelastic stress effects in the reservoir. Here, pore pressures in the reservoir blocks on both sides of the fault are gradually reduced from initial reservoir pressure up to the pore pressure at which the onset of rupture occurs. In our current approach, we do not explicitly model the process of reservoir depletion, which means production wells and associated sink terms have not been explicitly modelled. We here assume a homogeneous depletion of pore pressures in both reservoir compartments, which means production wells are not explicitly modelled and pressure gradients within the reservoir blocks are not accounted for. For depleting gas reservoirs in permeable sandstones (like the Groningen gas field), the assumptions of the absence of strong pressure gradients around the production wells and a homogeneous reservoir depletion are a simplified, but reasonable assumption. As the pore pressures in the reservoir decrease, the effective vertical stress increases and the volume of the reservoir rocks decreases due to compaction. For a laterally extensive reservoir, the vertical compaction of the rocks is mostly accommodated through subsurface deformation and ground subsidence. Total vertical stress changes within a laterally extended reservoir are therefore expected to be negligible and effective vertical stress changes within the reservoir are equal to the imposed pore pressure changes. As the reservoir rocks are juxtaposed to the rock volumes laterally bounding the reservoir, volume changes due to compaction cause

a reduction in total horizontal stress. The increase in the effective horizontal stress will therefore be smaller than the change in vertical effective stress. Hence, differential stresses in the reservoir will increase and may (depending on the Poisson's ratio of the rocks) lead to a stress path which destabilizes the faults (Zoback 2007). In case of fault offset, significant stress concentrations can develop along the fault, as differential compaction of reservoir compartments separated by the fault will lead to opposed shear displacements across the fault (Mulders 2003; Orlic & Wassing 2013).

We assume initial hydrostatic pore pressures in the caprock and burden, and a 5 MPa overpressured reservoir filled with gas (Verweij *et al.* 2012). We assume no hydraulic connectivity exists between reservoir, caprock and burden, which means during reservoir depletion pore pressures in rocks other than reservoir remain constant. Furthermore, as most of the faults within the Groningen sandstone reservoir are non-sealing, we presume that pore pressures in the fault segments which are juxtaposed against reservoir rocks follow the decline of pore pressures in the reservoir. Pore pressures in fault segments without reservoir contact are assumed to remain constant. Reservoir, underburden and caprock are represented by solid elements, characterized by elastic material behaviour. We consider both a model with and without stiffness and seismic impedance contrasts. The fault in the geomechanical model is composed of interface elements, and the initial fault strength is characterized by a Mohr Coulomb failure law, i.e.:

$$\tau_{max} = C + \mu_{stat}\sigma'_n \tag{1}$$

where τ_{max} is the maximum shear stress the fault can resist before failure occurs, C is fault cohesion, μ_{stat} is the static friction coefficient (which defines the friction coefficient just before the onset of failure) and σ'_n is the effective normal stress on the fault. A slip-weakening friction law was used in the geomechanical model (see Fig. 2) to model the post-failure evolution of friction during fault slip (Ohnaka 2013; Wassing *et al.* 2016; Buijze *et al.* 2017; Buijze *et al.* 2019).

3 THE EQUIVALENT FORCE FIELD METHOD: COUPLING DYNAMIC RUPTURE TO SOURCE-TIME FUNCTIONS FOR SEISMIC MODELLING

Here, a generic coupled modelling approach is described in which an arbitrary geomechanical and seismic wave propagation codes can be coupled (see scheme in Fig. 1). The geomechanics code is run in a multi-stage approach in which the static, dynamic and seismic stage are connected and coupled to the seismic wave propagation code. The resulting outcomes of geomechanical and seismic simulations are compared against one another.

3.1 Static stage (geomechanical model)

The first stage is run in quasi-static mode in a geomechanical model. Pore pressures in the reservoir rocks and adjacent fault segments are gradually decreased, ultimately resulting in a reactivation of the fault. When the static frictional resistance as defined by eq. (1) is exceeded, fault friction decays linearly with slip displacement until the dynamic friction μ_{dyn} is reached over a critical distance D_c, as illustrated in Fig. 2. Rock, fault properties and imposed initial stress and pressure conditions are shown in Table 1. In both cases, first fault reactivation occurs at a depth of 2900 m at the top of the hanging wall
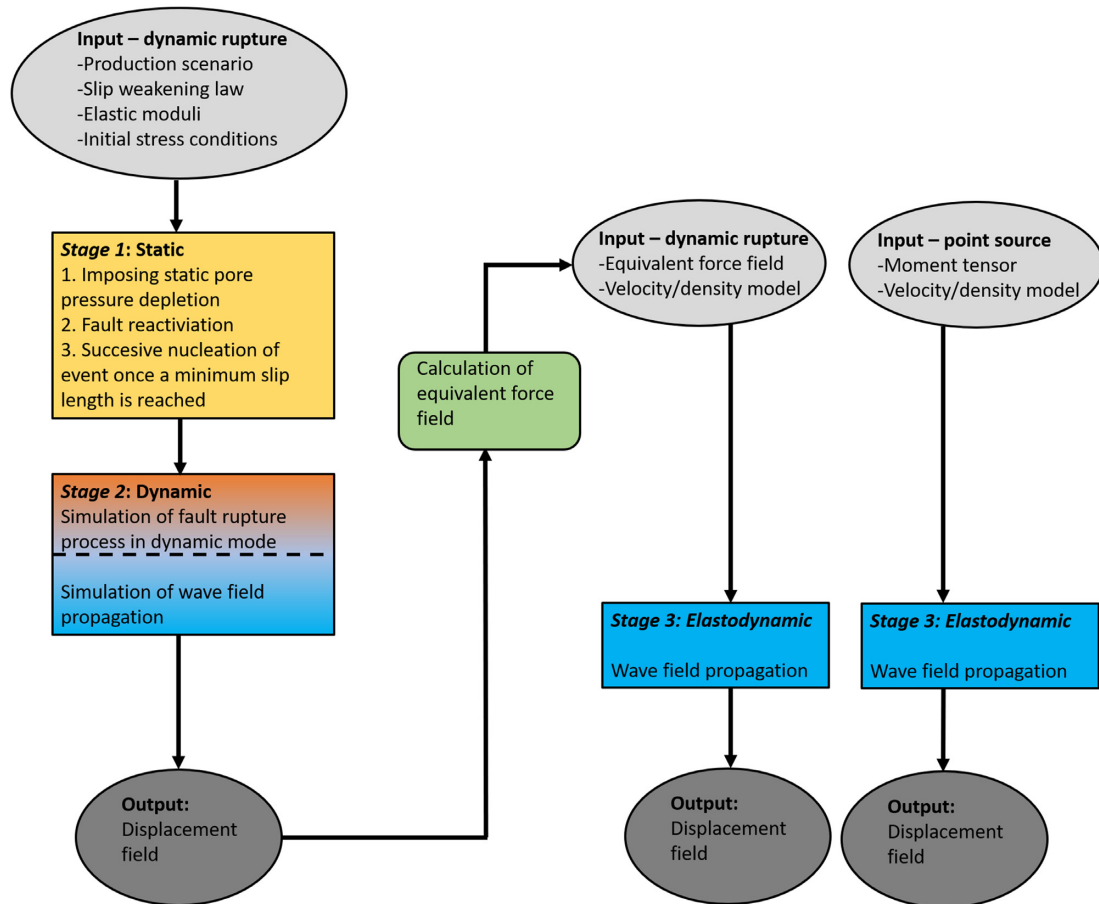
Figure 1. Flow chart describing the coupling of the geomechanical model to seismic wave propagation model. See sections 3.1–3.4 for a further explanation of the workflow.
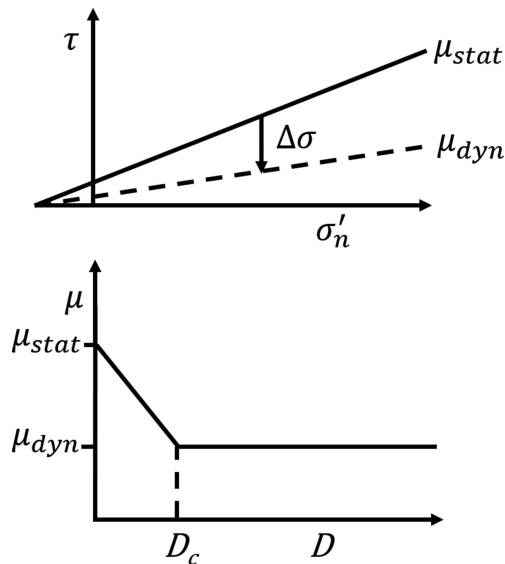

Figure 2. Illustration of the slip weakening law used for modelling evolution of fault friction during fault slip.

reservoir block. In the static stage prior to fault reactivation we can neglect inertia terms, as reservoir depletion by gas production takes place on a decade scale, with slow pore pressure loading on faults.

3.2 Dynamic stage (geomechanical model)

After reactivation of the fault, initially the increase in fault slip area and fault slip displacements is still controlled by the applied pore pressure loads. However, once a minimum slip length is reached (nucleation length), we observe a rapid increase in fault slip and slip area, indicative of the nucleation of a seismic event and the start of 'self-propagating' fault rupture. The theoretical nucleation length L_{nucl} for a slip-weakening rupture instability can be derived by eq. (13) of Uenishi & Rice (2003):

$$L_{nucl} = \frac{1.158\mu^*}{W} \tag{2}$$

Here we have the shear modulus $\mu^* = G/(1 - v)$ and weakening rate $W = (\tau_s - \tau_d)/D_c$, with G the shear modulus of the rocks, v Poisson's ratio, D_c critical slip distance, τ_s is shear stress on the verge of fault slip and τ_d is dynamic or residual shear stress. Common values were chosen for these parameters based on the work by Buijze *et al.* (2019), who evaluated the sensitivity of reactivation and rupture size to these parameters. Both the model without and with velocity contrasts have an initial pressure at the top of the reservoir (2800 m depth) of 35.2 MPa. Self-propagating fault rupture starts at a pore pressure depletion of 5.8 MPa and 9.6 MPa in the model without, resp. with velocity contrasts, at a nucleation length of approximately 50 m. Subsequently a shift is made to the dynamic stage in the geomechanical model, to simulate the evolution of the successive time-dependent rupture process along the

Table 1. Parameterization of the homogeneous model and layered model. The upper table gives stress gradient, pore pressure gradients and fault frictional parameters for both the model without and with acoustic impedance. Note that for the Zechstein lithology a high horizontal stress gradient is used, to simulate the isotropic stress conditions in the Zechstein rock salt. Lower table gives density, elastic properties and resulting wave velocities.

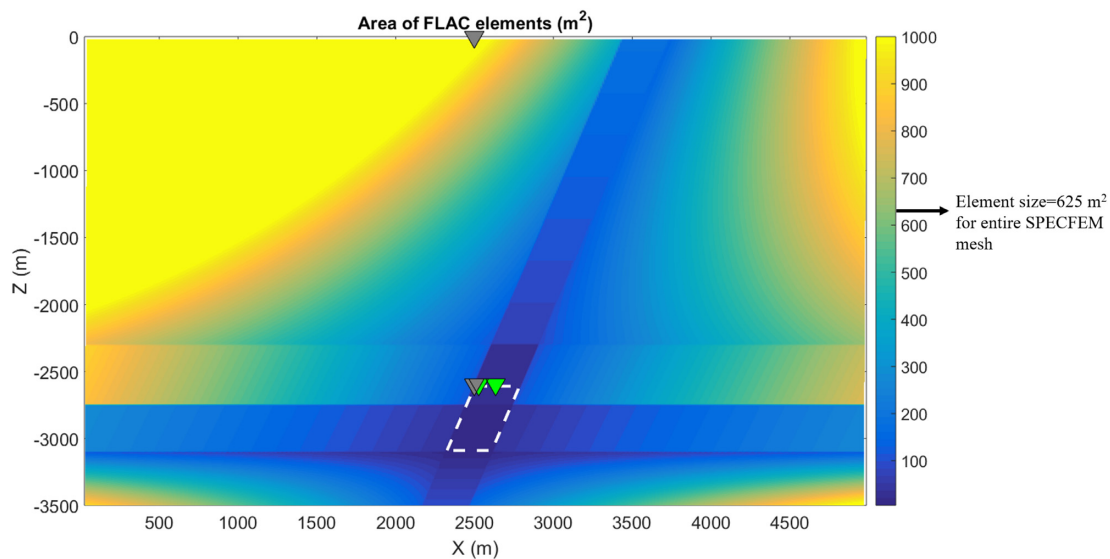|	Geological Unit	Stress gradient Vertical/horizontal (10^4 Pa m^{-1})	Pore pressure gradient (10^4 Pa m^{-1})	Friction coefficient ($\mu s/\mu d$) (-)	Fault Dc (m)	
Homogeneous model and layered model	Overburden	2.16/1.60	1.10			
	Zechstein	2.16/2.16	1.10			
	Rotliegend (reservoir)	2.16/1.60	0.18			
	Carboniferous	2.16/1.60	1.10			
	Fault			0.60/0.45	0.01	
	Geological unit	Young's modulus (E, GPa)	Poisson's ratio (v, -)	P-wave velocity (Vp, m/s)	S-wave velocity (Vs, m/s)	Density (ρ, kg/m^3)
1. Homogeneous model	Uniform	30	0.17	3828	2414	2200
2. Layered model	Overburden	10	0.25	2449	1414	2000
	Zechstein	35	0.30	4737	2532	2100
	Rotliegend (reservoir)	30	0.17	3831	2413	2200
	Carboniferous	40	0.25	4297	2481	2600

Figure 3. Map showing the spatial distribution of the area of elements in FLAC. In SPECFEM we defined a uniform element area of 100 m². The two green triangles at 2600 m depth mark the positions from synthetic receivers depicted in Figs 7 and 12. The two grey triangles at, respectively, 2600 and 0 m depth, mark the location from synthetic receivers shown in Fig. 10. The position of the source region considered in this study is highlighted by the dashed white line.

fault. After nucleation, the rupture propagates downwards, where the length of the fault patch affected by slip after fault rupture is around 120 m. The rupture process induces temporal variations in the seismic displacement field. This displacement field is stored as a function of time at a densely spaced grid within the source region. It is noted here that the length of the nucleation fault patch (Uenishi & Rice 2003) and the rupture process itself have been shown to be dependent on parameters like fault offset, initial tectonic stresses and the fault slip-weakening parameters, and will affect the seismic waveforms (Buijze *et al.* 2019).

3.3 Elastodynamic stage (seismic model)

Key to our approach is the transportation of the seismic displacement field of the geomechanical model into the seismic model. The challenge is that there are many differences between the physical properties of the two models. First, in the immediate surroundings of the source area there is a difference in the constitutive equation,

most notably the transient failure of the fault during the rupture in the geomechanical model. But also, the structural geometry and physical properties will in general be different. The geomechanical model will be more detailed than the smoother elastodynamic model, while the elastodynamic model may contain features that are not so relevant for the geomechanical model. As a result, the wave field displacements obtained from the geomechanical model do not satisfy the equations of motion in the seismic model. Therefore, the displacements cannot simply be copied from one code to the other.

One possible approach is to define a bounding box around the source area, such that the geomechanics code takes care of the physics inside the box, while the seismic wave propagation code takes care of the wave propagation outside. The communication can then be done by recording the outgoing wavefield (displacements and normal derivatives) of the geomechanics code on the bounding box, and subsequently using this as a boundary condition for the seismic wave propagation code. However, this has a
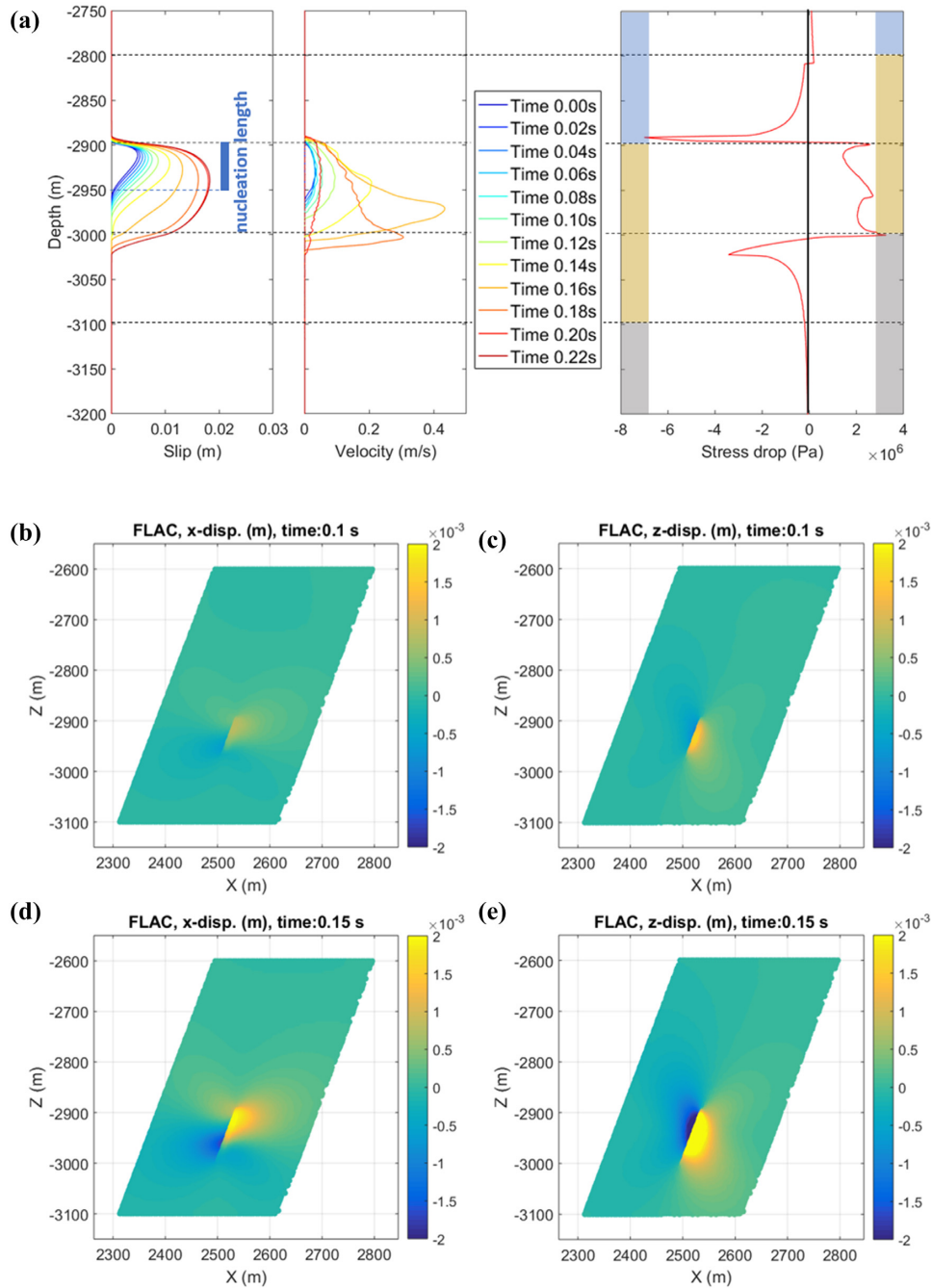
Figure 4. Results of the geomechanical model described in Table 1. (a) Profile along the fault plane of the fault slip, fault velocity resulting from dynamic fault rupture within the geomechanical FLAC model. Additionally the geological schematization is shown by the colored column, with from bottom to top the Carboniferous (grey), Rotliegend (brown) and Zechstein (blue). (b) and (c) Snap shots of horizontal and vertical displacement fields (m) at time 0.1 s. (d) and (e) Snap shots of horizontal and vertical displacement fields at time 0.15 s. Note that uniform elastic constants are assigned throughout this entire model, thus no seismic impedance contrasts are present.

notable disadvantage as the isolated fault region will be unavailable for wave propagation in the seismic wave propagation code and may therefore cause artefacts in the resulting displacement fields.

Instead we propose to use the concept of the equivalent body-force density also known as equivalent force field as introduced by Backus & Mulcahy (1976), which implies that any displacement field in the subsurface can be expressed by an equivalent force

field according to the equation of motion, which is explained in the following.

Let us define L as an operator that represents the linear (seismic) wave equation. It's operation on a (vector) displacement field u with components u_i is defined as:

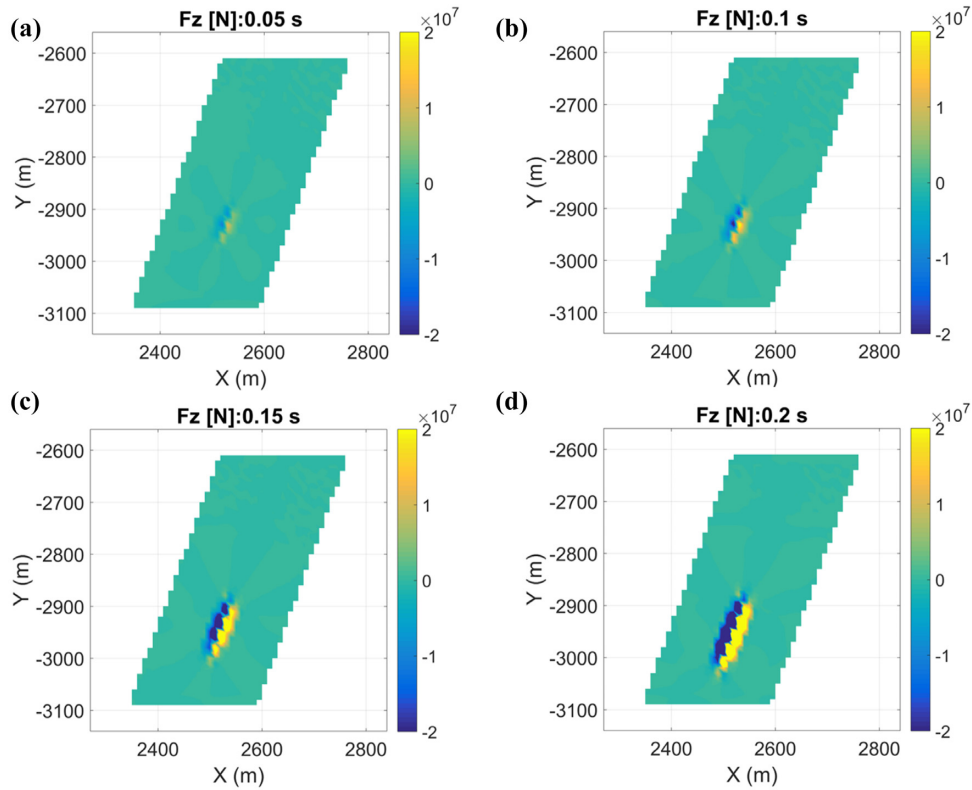$$(Lu)_i = \rho \partial_t^2 u_i - \partial_k c_{ijkl} \partial_j u_l \qquad (3)$$

Figure 5. Vertical component of the equivalent force field (N) calculated from displacements of the homogeneous FLAC model at four successive times: (a) $t = 0.05$ s, (b) 0.1 s, (c) 0.15 s and (d) 0.2 s.
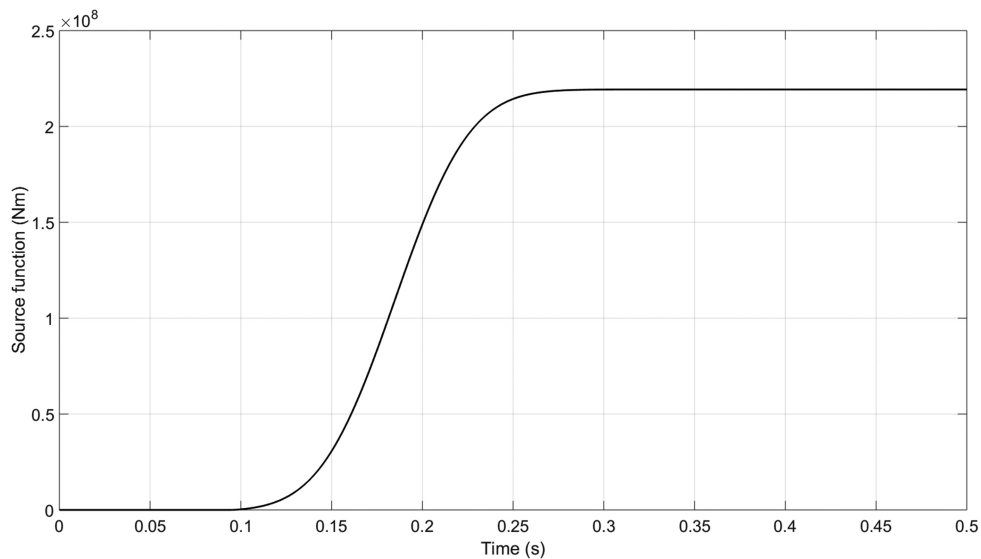

Figure 6. Source-time function used for the moment tensor definition for the homogeneous case.

with mass density ρ, time t and elasticity tensor c_{ijkl}. For any displacement field w_i that uniformly satisfies the homogeneous seismic wave equation the following holds:

$$(Lw)_i = 0. \qquad (4)$$

In the geomechanics code, the constitutive equation will be more general than simply linear elastic and may include non-linear elements such as a non-linear slip weakening law along a fault. We define v as the (incremental) displacement field as calculated in the geomechanics code, relative to the displacement field at the start of the dynamic phase. This field may be thought of as being the solution to a more general, non-linear operator G acting on v, such that $(Gv)_i = g_i$, where g may represent any external forcing. However, the precise definition of G and g is not relevant in the following, as long as the resulting geomechanics displacement field v is available.

The displacement field v will in general not satisfy the seismic wave equation. Therefore, when we apply the seismic operator L to
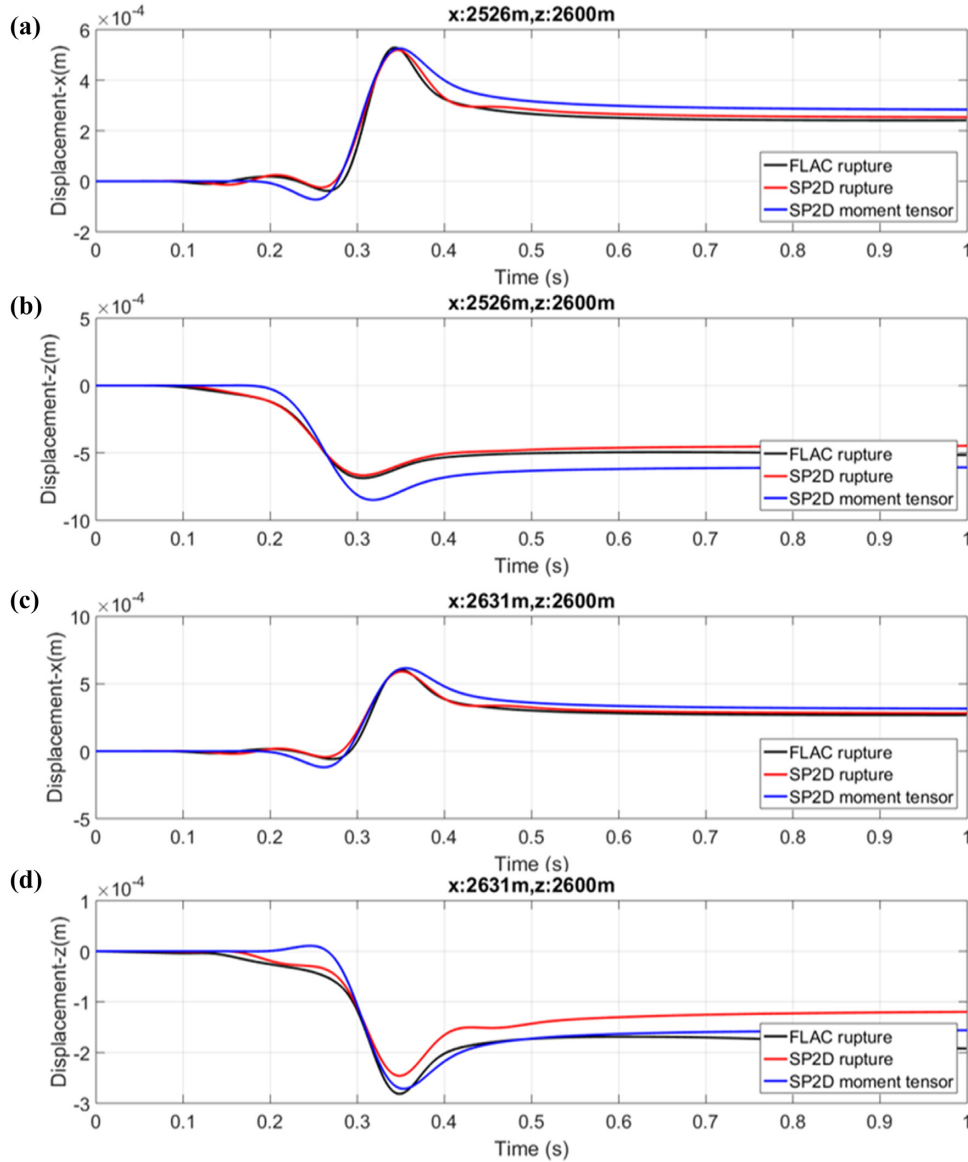
Figure 7. Comparison for the homogeneous model between displacements from FLAC with rupture (black), SPECFEM with rupture adopted from FLAC (red) and SPECFEM with a point source moment tensor (blue). Displacements at two nodal points at $x = 2526$ m (a, b) and $x = 2631$ m (c, d) at 2600 m depth are shown. (a) Horizontal displacements at $(x, z) = (2526, -2600)$. (b) Vertical displacements at $(x, z) = (2526, -2600)$. (c) Horizontal displacements at $(x, z) = (2631, -2600)$. (d) Vertical displacements at $(x, z) = (2631, -2600)$. The SPECFEM displacement curves (red and blue) are scaled with respect to the peak displacement of the FLAC displacement. A lowpass filter with high cut frequency of 15 Hz was applied to the data. The position of these synthetic receivers is shown by the green triangles in Fig. 3.

v this will result in a spatiotemporal misfit field, that we represent by the symbol f:

$$(Lv)_i = f_i. \tag{5}$$

This misfit field f has the physical dimensions of a force field and is called the equivalent body-force density field, or simply equivalent force field. As such, it can explicitly be used as a forcing term in the seismic wave equation. We may then define u as the solution to the inhomogeneous wave equation to be solved by the seismic wave propagation code:

$$(Lu)_i = f_i . \tag{6}$$

Combining eqs (5) and (6) reveals that:

$$(Lu)_i = (Lv)_i \tag{7}$$

and thus that the solution u of the seismic model equals the incremental displacement field from the geomechanical model, with a possible superposition of any arbitrary displacement field w that satisfies the homogeneous linear wave eq (3).

$$u = v + w. \tag{8}$$

This expresses the advantage of the equivalent force approach relative to approaches that impose the displacement field directly. One may think, for example, of a reflector beneath the reservoir, that sends reflected waves back through the source region. Even if the reflector is not present in the geomechanical model, and therefore its effects not present in the geomechanical displacement field v, it will still be properly accounted for in the seismic propagation model, at least to the extent that its effects are purely linearly elastic (seismic).
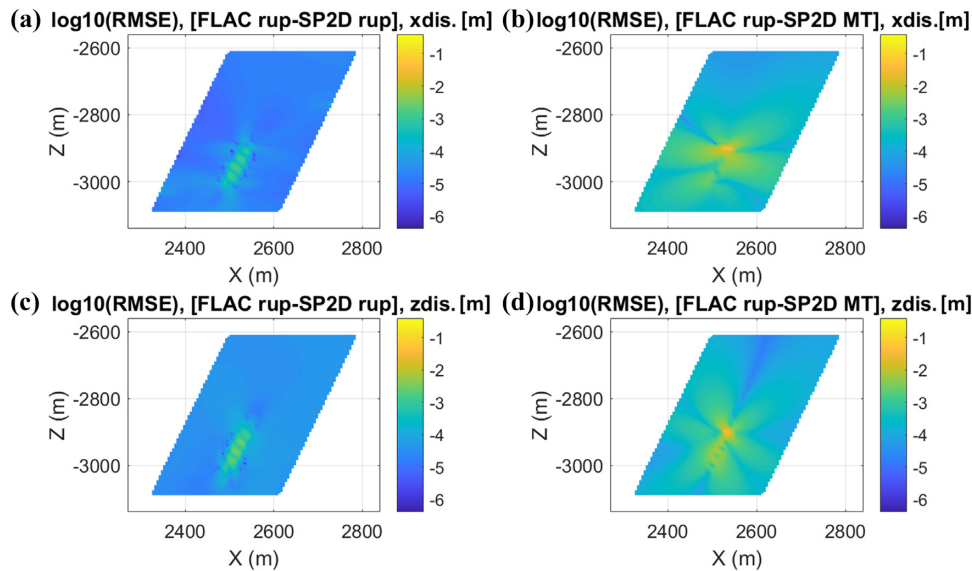
Figure 8. Plot of the logarithm of the root-mean-square-error of the displacement field throughout the source region. Note that we used logarithmic scaling to enhance variations of RMSE. (a) $\log_{10}$(RMSE) from FLAC rupture model with SPECFEM rupture model for horizontal component. (b) $\log_{10}$(RMSE) from FLAC rupture model with SPECFEM moment tensor model for horizontal component. (c) $\log_{10}$(RMSE) from FLAC rupture model with SPECFEM rupture model for vertical component. (d) $\log_{10}$(RMSE) from FLAC rupture model with SPECFEM moment tensor model for vertical component. Note that we used logarithmic scaling to enhance variations in RMSE.
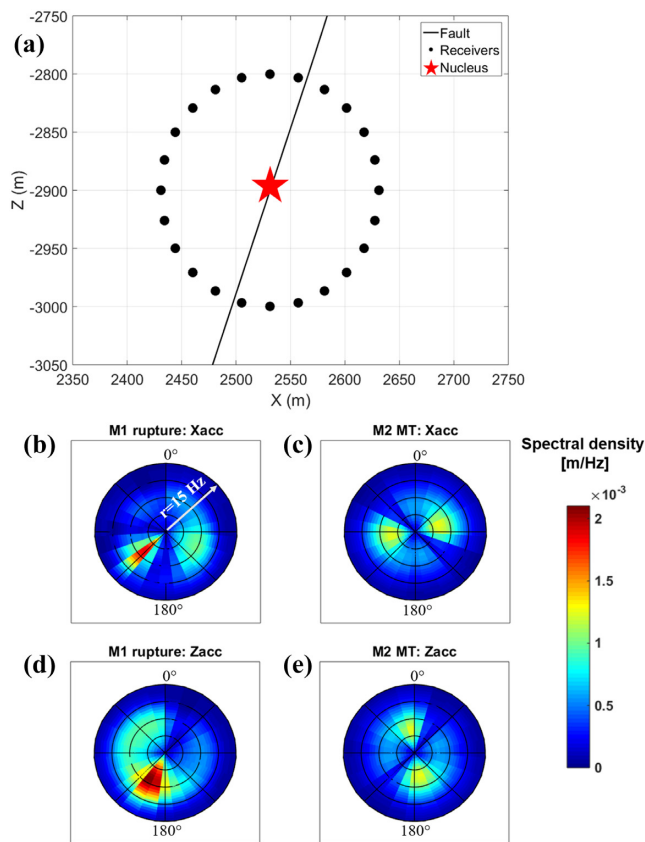

Figure 9. Polar plots of the frequency content for synthetic receivers distributed spherically at 100 m from the centroid. The radius of the polar plots ranges from 0 to 15 Hz and the incremental angle of receivers is $15°$. (a) Geometry of receiver distribution in the model. (b) Horizontal component of rupture simulation. (c) Horizontal component of moment tensor simulation. (d). Vertical component of rupture simulation. (e) Vertical component of moment tensor simulation.

It should be noted that the approach does not only account for differences in the type of constitutive equation (i.e. linear versus non-linear), but also for differences in the linear domain only. Differences in the spatial distribution of elastic parameters and densities are expected based on different requirements of model representation in the geomechanics and the seismic models. In general, one can expect the geomechanic model to be more detailed within the source area, but possibly less detailed outside.

Note that in our calculations we choose to use undrained moduli (i.e. dynamic moduli), which is further explained in the Appendix.

3.4 Point source moment tensor simulation in seismic model

Additionally, we compare the outcomes of the rupture simulations against a point source simulation to address their differences in spatio-temporal wavefield variations. Here, we represent the actual rupture process by a double-couple point source which is a common earthquake source representation in seismic wave propagation models. The moment tensor elements are calculated from the strike, dip and rake using the relationship for a shear dislocation of arbitrary orientation (Aki & Richards 2002). The point source was positioned at the centroid, which is the center of the rupture area in the geomechanical model. The source time function corresponds to a Heaviside function with an onset-time and frequency content based on the displacement field characteristics in the rupture zone. Note that the onset-time is non-zero due to imposed pore-pressure depletion in the static phase.

3.5 Model considerations and specifications

To demonstrate our approach we use FLAC and SPECFEM to, respectively, conduct the geomechanical and seismic calculations within the coupled modelling approach. We will consider both a homogeneous model and a layered model, and their respective
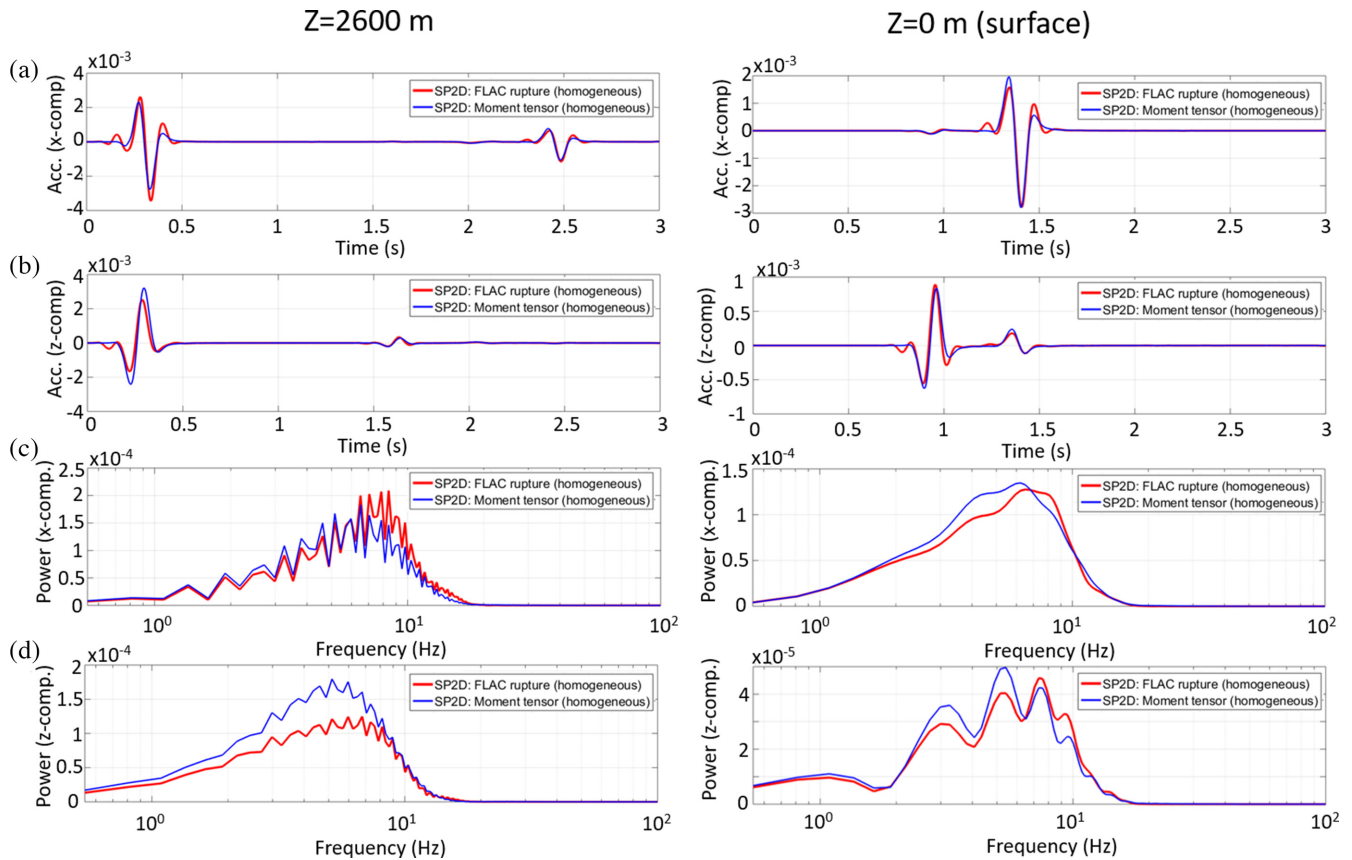
Z=2600 m

Z=0 m (surface)

Figure 10. Comparison between the rupture- (red) and moment tensor (blue) simulations showing the waveform accelerations and frequency spectra for central synthetic receiver ($x = 2500$ m) at $z = 2600$ m (left-hand column) and z = 0 m (right-hand column). (a) Horizontal component. (b) Vertical component. (c) Frequency spectrum horizontal component. (d) Frequency spectrum vertical component. The true amplitudes are preserved, and data are unscaled. The position of these synthetic receivers is shown by the grey triangles in Fig. 3.

parametrization of fault properties and stress conditions, pore pressure gradients, densities and elastic constants are given in Table 1. To make our application more specific we focus on the Groningen gas field case, and include specific knowledge on dynamic rupture process and geology in our study. The layered model is a simplification of the subsurface composition at the Groningen gas field, with differentiation of the major geological units having *in situ* stress and pore pressure conditions and geomechanical values representative for this site. For the homogeneous model we used average elastic constant values based on the layered model. Note that in both models high initial horizontal stress gradients are imposed on the Zechstein rock units, which will limit the rupture in upward direction. Rupture in upward direction is expected to be limited due to isotropic stress conditions in the Zechstein unit, caused by the presence of viscoelastic rocksalt.

In FLAC3D an irregular mesh was defined with finest elements along the active fault region of 5 m², and coarsest at the model boundaries of 9180 m². In SPECFEM a regular grid with elements of 625 m² was defined. In the analysis, we study frequencies up to 15 Hz, where we use a spatio-temporal discretization in FLAC and SPECFEM mesh that meet the sampling criteria holding in SPECFEM and FLAC (Itasca 2013; SPECFEM2D User Manual 2015).

Both the FLAC (FEM) and SPECFEM (SEM) models maintain absorbing boundary conditions at the bottom and side boundaries and free-surface condition at the top of the model. The insertion of an equivalent force field in a limited source area does not affect

or include boundary conditions, since there are no continuity requirements on a force field. In both models anelastic attenuation is ignored.

In FLAC we neglect both mass-dependent damping which applies for low frequency instabilities, as well as stiffness-dependent damping that applies for high frequency numeric instabilities (Itasca 2013). Based on separate tests for the considered model in FLAC, we observe that the frequency content up to 15 Hz is not affected by numerical noise related to the neglection of either type of damping.

When material property contrasts are limited, which is the case in our model, the continuous Galerkin technique as implemented in SPECFEM is sufficient to accurately conduct seismic simulations. In the layered model we define a conforming mesh where the element boundaries follow the interfaces, such that material interfaces never intersect the elements. For cases with more extreme contrasts in material properties, the discontinuous version of SEM can be used.

3.6 Numerical implementation of equivalent body force insertion

The spatial and temporal discretization of the FLAC model was chosen such that, in the far-field, ground motions with frequencies up to 15 Hz can be accurately simulated. However, in the near field, more resolution is required to capture the dynamic rupture process. To this end, the spatial discretization is marked by highest resolution
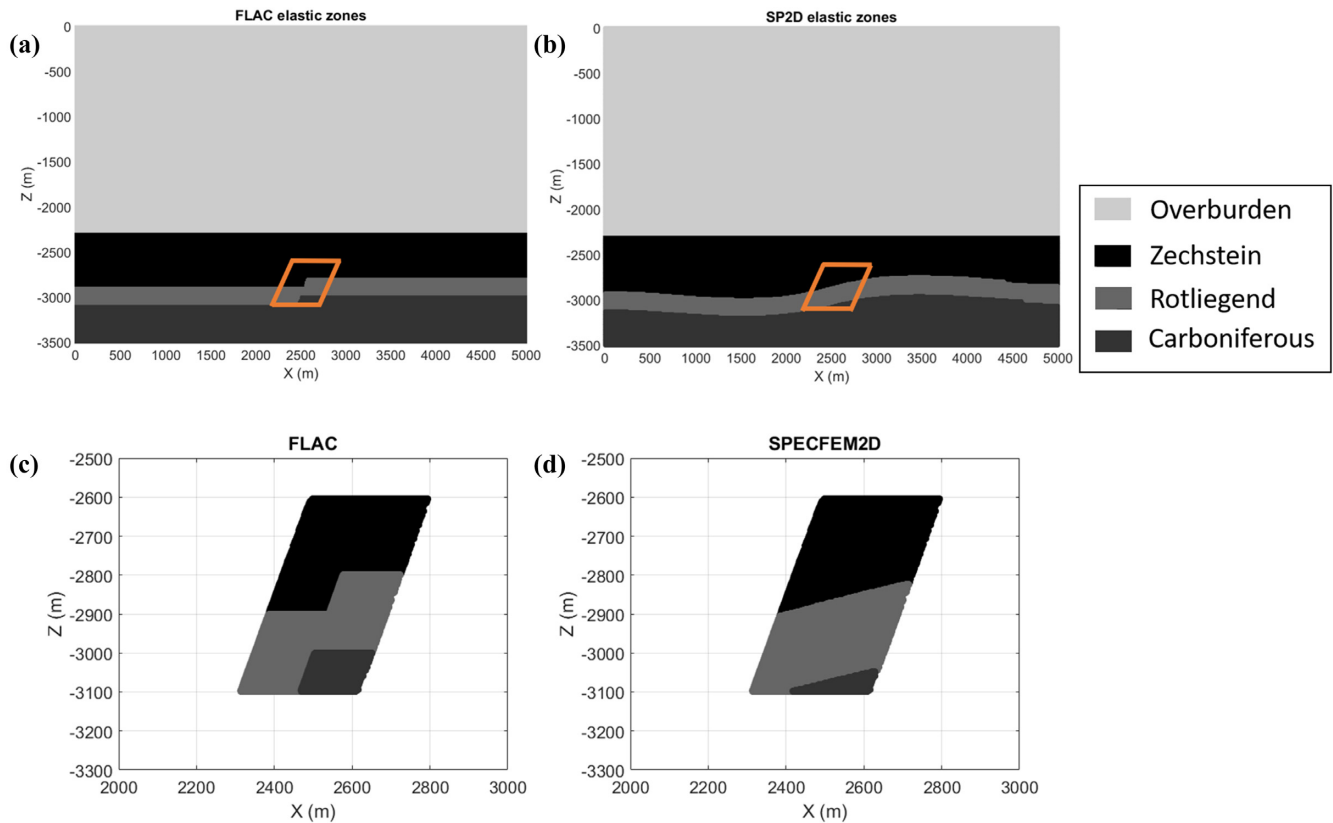

Figure 11. Comparison of layered velocity model as designed in FLAC and SPECFEM. (a) Entire model in FLAC. (b) Entire model in SPECFEM. (c) Selected source region in FLAC. (d) Selected source region in SPECFEM. See Table 1 for elastic property values of the four layers.

close to the source, and the time step used within the dynamic stage of the FLAC simulation is very small (2.5×10^{-5} s).

For the conversion from the displacement field calculated by FLAC to the equivalent force field released in SPECFEM we have used the following steps:

(1) First, the displacement time-series were collected from the dynamic FLAC simulation nodal output within the source region, corresponding to the corner nodes of the elements in the FLAC grid. Due to the variations of element dimensions in the FLAC grid (see Fig. 3), the spacing between neighbouring nodes varied throughout the model. At this point, the time-series were resampled to a coarser temporal discretization to reduce data-dimensions, while still sufficient for sampling the frequency content of interest, and to allow filtering as proposed in step 4.

(2) Next, the displacement field from the geomechanical model v_j was mapped from the dense, non-equidistant FLAC grid to the coarser, equidistant rectangular grid that was used in the SPECFEM simulations. A triangulation-based cubic interpolation method is used to regrid the data which produces a smooth surface. The cubic interpolation is generally accepted as excellent representation to capture second order derivatives in displacement (e.g. Zienkiewicz & Taylor 2000). This interpolation approach worked adequate for our examples, although in other applications, it may be necessary to use an integral averaging or smoothing approach.

(3) Next, the equivalent force field terms f_i in eq. (6) (with suffix i for dimensions x and z) were calculated. Since we applied a rectangular, equidistant grid in SPECFEM, the derivatives were calculated by finite differences. The temporal and spatial derivatives

within eq. (6) were calculated with the central difference method such that:

$$\frac{\partial v_i^n}{\partial t} = \frac{v_i^{n+1} - v_i^{n-1}}{2\Delta t} \tag{9}$$

$$\frac{\partial v_l^n}{\partial x} = \frac{v_l^{n+1} - v_l^{n-1}}{2\Delta x}. \tag{10}$$

(4) Finally, the equivalent force fields were low pass filtered with a second order Butterworth filter with a high-cut frequency of 15 Hz, since we only consider frequencies below this value in this study. Next, the force fields were resampled using a cubic interpolation method to meet the time sampling conditions required for the SPECFEM simulation.

4 RESULTS

4.1 Homogeneous model

To demonstrate the reliability of the coupled modelling approach, we first consider FLAC and SPECFEM models that have identical homogeneous elastic properties, but different mesh properties. Fig. 3 shows the geometry of the homogeneous model.

Fig. 4(a) shows the result of the FLAC simulation with fault slip and velocity as a function of time. Figs 4(b)–(e) show the resulting displacement field for the horizontal and vertical component for two instances of time. The resulting displacements within the source region were converted to equivalent force terms using eq. (5). Fig. 5
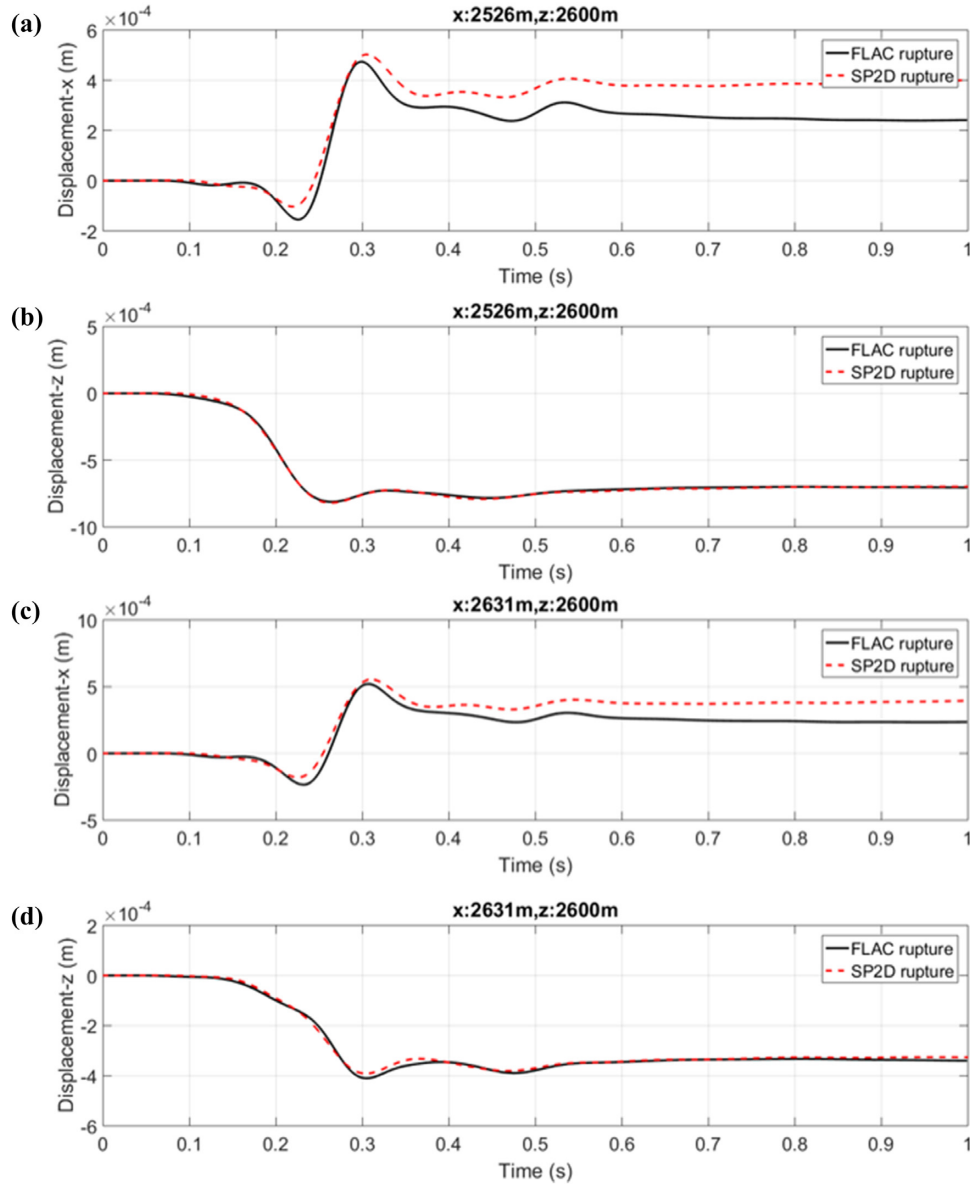
Figure 12. Comparison between displacements obtained from simulations in the layered model from FLAC3D (black) with SPECFEM with rupture adopted from FLAC (red dashed). Displacements at two nodal points are shown. (a) Horizontal displacements at $(x, z) = (2526, -2600)$. (b) Horizontal displacements at $(x, z) = (2631, -2600)$. (c) Vertical displacements at $(x, z) = (2526, -2600)$. (d) Vertical displacements at $(x, z) = (2631, -2600)$. The SPECFEM displacement curves (red) are scaled with respect to the peak displacement of the FLAC displacement. A low-pass filter with high cut frequency of 15 Hz was applied to the data. See Fig. 11 for model geometry. The position of these synthetic receivers is shown by the green triangles in Fig. 3.

shows the vertical force field (Fz) at four successive times, expressing the downward propagation of the rupture with time. The area with elevated force values is restricted to a narrow zone revealing the active part of the fault. With increasing distance to the fault, the force field quickly attenuates.

The equivalent force fields are used as source terms in the homogeneous SPECFEM model. Synthetic receivers were placed at a nodal grid surrounding the source region, with 10 m spacing between the receiver in the horizontal and vertical direction. To compare the outcome of the rupture simulation against a conventional point source representation, we additionally conducted a moment tensor simulation in SPECFEM. Based on strike $= 180°$, dip $= 70°$ and rake $= -90°$ the moment tensor in Cartesian coordinates is

expressed by:

$$M = M_0 \begin{pmatrix} M_{xx} & M_{xz} \\ M_{zx} & M_{zz} \end{pmatrix} = M_0 \begin{pmatrix} -0.6428 & 0.766 \\ 0.766 & 0.6428 \end{pmatrix}$$

Fig. 6 shows the source-time function that was defined to represent the actual rupture pattern, according to the procedure described in Section 3.4

Resulting displacements obtained with the moment tensor simulation are shown by the blue curves in Fig. 7. A clear resemblance is observed between displacements resulting from the rupture simulation (black and red) and those of the point source moment tensor (blue). Note however, that the point source representation is an
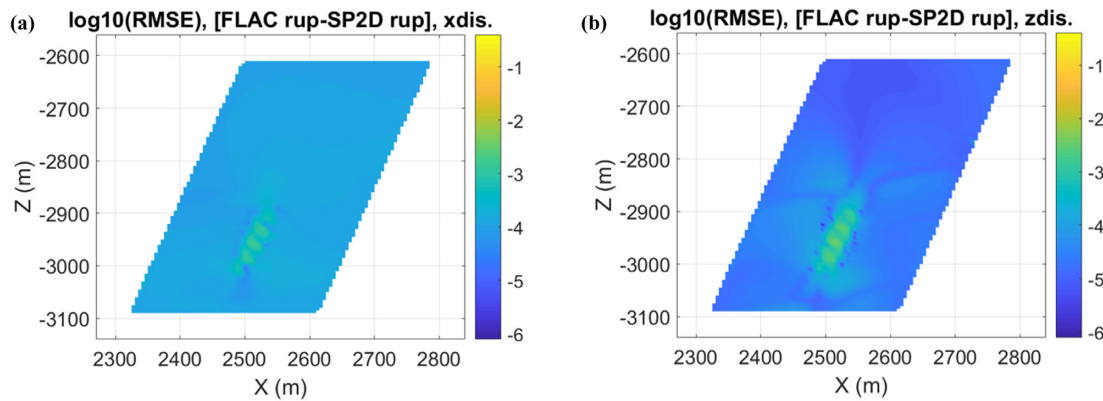
Figure 13. Maps of the logarithm of RMSE for the layered model. (a) RMSE of horizontal component, (b) RMSE of vertical component. The RMSE is plotted on a logarithmic scale within the same range as the RMSE plots from Fig. 8.

approximation of the actual rupture mechanism. Therefore, subtle differences in displacement curves are observed in Fig. 7 between the rupture and moment tensor simulation.

To quantify the performance of the two different SPECFEM simulations with respect to the FLAC simulation, we calculated the root mean square error (RMSE) at a nodal point grid in the source region.

At a given nodal point, the RMSE is defined by:

$$\text{RMSE} = \sqrt{\frac{\sum_{i=1}^{n} (F_i - S_i)^2}{n}}, \tag{11}$$

where F is the target value given by the displacement at time step i of the FLAC rupture simulation, S_i is the displacement at time step i of the SPECFEM simulation, n is the number of time-series pairs to compare.

Fig. 8 shows maps of RMSE in the area surrounding the source region for the horizontal and vertical displacements. RMSE (see eq. 11) is calculated with F_i as the FLAC output displacements and S_i SPECFEM displacements, either resulting from the equivalent force field simulations (termed *FLAC rup—SP2D rup* in Figs 8a and c) or the moment tensor simulations (termed *FLAC rup—SP2D MT* in Figs 8b and d). The RMSE is plotted on a logarithmic scale to enhance visualization. Fig. 8 shows that RMSE (*FLAC rup—SP2D rup*) is significantly lower compared to the RMSE *FLAC rup—SP2D MT*, both for the horizontal -and vertical displacement, with increased RMSE values near the center of the active fault part. The RMSE accentuates the mismatch in total displacement field between the FLAC rupture and SPECFEM moment tensor simulation (Figs 8b and d). Moving away outward from the fault zone the RMSE *FLAC rup—SP2D MT* do strongly diminish.

To compare the near-field frequency characteristics between the rupture and moment tensor simulations, we consider the frequency spectrum in the source region at receiver positions distributed radial symmetric from the center of the rupture area in the FLAC3D model with 100 m radius. We consider frequency spectra of the horizontal and vertical accelerations for the *SP2D rup* simulation against the *SP2D MT* simulation within the time window of 0–0.5 s. The angle between successive receivers with respect to the source origin was incremented by 15° (see Fig. 9a). The frequency spectra are visualized in polar plots in Figs 9(b)–(e), where the radius ranges from 0 to 15 Hz. Fig. 9 shows that the rupture spectra have a different expression as a function of angle compared to the moment tensor spectra. The rupture spectra of the two components clearly reach their peak power near 225° and 200°, for the horizontal and

vertical component, respectively. The point source simulation shows a different directionality having two peaks that are smaller and radial symmetric near 70° and 250° for the horizontal component, and near 170° and 350° for the vertical component. Additionally, differences in dominant frequency are observed between the two simulations, where it ranges from 5 and 10 Hz for the *SP2D rup* and between 5 and 8 Hz for the *SP2D MT* simulation.

Fig. 10 shows acceleration waveforms and frequency content for the central receiver along the reference line at $z = 2600$ m (left-hand column) and at $z = 0$ m (right-hand column). Note that the signals arriving at 2.5 and 1.5 s for the x and z component at 2600 m depth are free-surface reflections from the top surface. At 2600 m depth P and S phases are not visually distinguishable, because their relative phase shift is too small at this bandwidth. On the surface (0 m), the P and S phases can be clearly distinguished and are more clearly expressed on the vertical and horizontal components, respectively. Fig. 10 shows that with distance increasing from the active fault segment the accelerations obtained from the rupture simulation and point source show only subtle amplitude and phase difference, though the rupture accelerations have a slightly higher peak frequency value compared to the moment tensor accelerations.

4.2 Layered model

We now consider a layered elastic model based on of the dominant geological units present in the Groningen gas field. The parametrization of elastic constants for the layered model is given in Table 1. Fig. 11 shows a comparison of the models as implemented in FLAC and SPECFEM. In FLAC (Figs 11a and c) we defined the actual fault geometry with offset between adjacent geological units. In SPECFEM (Figs 11b and d) we make a simplification of the FLAC geometry and replace the discontinuity at the fault by a gentle fold, resulting in a different spatial distribution of elastic constants. According to eqs (5) and (6) our approach compensates for the difference in the elastic field encountered at the source region between the FLAC and SPECFEM model.

We made similar comparisons between waveforms as for the homogeneous case in the same bandwidth, with results depicted in Figs 12 and 13. Fig. 12 showing comparison of displacements at 2 nodes at 2600 m depth, illustrating an overall high similarity between the *FLAC rup* and *SP2D rup* simulations. Although the vertical displacement shows an excellent match, small differences are observed for the horizontal displacements with the *SP2D*
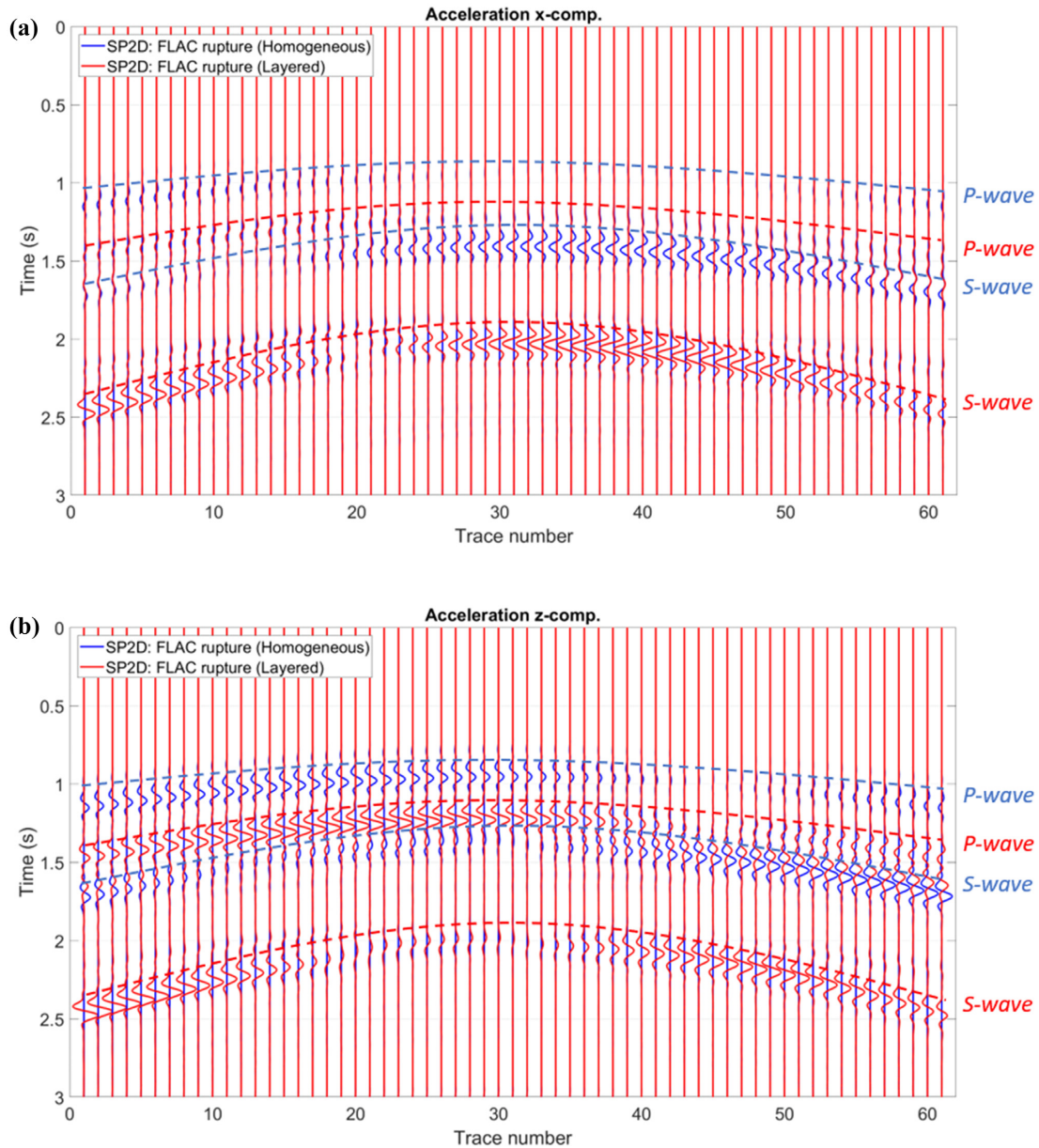
Figure 14. Surface accelerations (m s^{-2}) at 0 m of SPECFEM with rupture adopted from FLAC3D for the homogeneous case (blue) and layered case (red). (a) Horizontal component and (b) vertical component. First arrivals of *P* waves and *S* waves are indicated by the dashed lines with blue and red for the homogeneous and layered case, respectively.

rup displacements reaching higher displacements at later arrival times compared to *FLAC rup* displacements (Figs 12a - d). Such differences are related to approximations made in the calculation procedure of the equivalent force field from the FLAC displacement field. The RMSE maps depicted in Figs 13(a) and (b) for the horizontal and vertical component show a similar range as for the homogeneous case (Figs 8a and b), with strong RMSE decay directly outside the active fault segment. Fig. 14 shows a panel of surface accelerations on the horizontal and vertical component for the homogeneous (blue) and layered case (red). Here the *P* phase and *S* phase can be clearly distinguished on the vertical- and horizontal component, respectively, as indicated in Fig. 14 by the dashed lines. A significant difference in arrival times and waveforms is observed for the two different cases, with the *P* and *S* phase observed for the layered case having a time delay compared to the homogeneous

case, related to the difference in material property distribution for the two cases.

Overall the strong agreement in displacement fields for the layered case between the original FLAC rupture simulation and the SPECFEM simulation with adopted rupture shows that the equivalent force terms successfully compensate for a difference in distribution of elastic constants between the two models (Fig. 12) and is not hampered by different mesh resolutions.

5 DISCUSSION

Our results show that we can successfully couple a geomechanical model to a seismic wave propagation model. Our approach translates the displacement field resulting from geomechanical simulation into equivalent force terms within the active source region,

which is subsequently inserted into a coarse and simplified mesh of a wave propagation model. At locations in the model where the equation of motion is non-zero, a force term is imposed such that equilibrium is reached. We verify the approach by comparing displacements obtained from a FLAC to SPECFEM displacements in an area embedding the active source region based on an equivalent force field. The method we propose accurately represents the displacement field that was calculated by FLAC.

Performance analysis of the model results show low RMSE values for both the homogeneous and layered model with the rupture source mechanism inserted in SPECFEM (Figs 8 and 13). Minor differences are observed between the FLAC- and SPECFEM displacement fields, related to the approach used to upscale the FLAC grid to the SPECFEM grid. The SPECFEM grid is a coarsened representation of the continuous representation of the displacement field from FLAC that is accurate to the second order. Although the cubic interpolation method produces an overall smooth representation of the displacement field, subtle differences in displacement fields between FLAC and SPECFEM outcomes are introduced (Figs 7, 8, 12 and 13). Although a thorough investigation of the effects of numerical approximations is beyond the scope of this study, we anticipate that more advanced upscaling procedures, such as expressing the displacement field by a surface integral, can even further reduce these differences. The results demonstrate that the method can be successfully applied for more complex geological settings to address near and far-field expression of realistic rupture mechanisms. The comparison between the rupture simulation and moment tensor simulation show differences in waveform shape, phase and frequency. Although these differences are most clearly expressed in the source region, differences are also observed at shallower depths (Fig. 7).

The FLAC simulations did not include low- or high frequency attenuation. Based on diagnostics we did not encounter distortions from low-frequency attenuation. However, we did notice that above 15 Hz high frequency oscillation occurs in the FLAC displacements, which is why we used a 15 Hz low-pass filter. However, this prevents us from studying signal content of frequencies above 15 Hz. Future studies should address the value of higher frequencies contained in far-field observables and check if these contain additional information of the complex source mechanism as compared to observables from point source simulation.

Our approach is specifically developed for modelling of induced earthquakes with the main advantage of using a dedicated geomechanical package (e.g. FLAC3D, DIANA) to model the geomechanical response of the reservoir due to the spatial and temporal changes in the reservoir, and the specific reservoir and fault geometry. This results in a typical reactivation pattern of the faults which may result in induced seismicity with a typical rupture pattern and specific seismic wavefield characteristics. The approach has the benefit of combining a realistic source representation contained in a geomechanical package with the computational efficient spectral element method used in a wave propagation package to calculate far-field observables.

6 CONCLUSIONS

We demonstrated an approach to couple geomechanical models to seismic wave propagation models, consisting of three stages. First, a geomechanical modelling package is used to calculate the time-dependent displacement field in the source region. Next, the displacement field is converted to an equivalent force field using the

equation of motion. Subsequently, the equivalent force field is released in a seismic modelling package to conduct wave propagation simulations to the surface. We tested this approach using the geomechanical and seismic modelling packages FLAC and SPECFEM, respectively. The results of the homogeneous model where we included a comparison to a point source representation show a high correlation between the original FLAC and derived SPECFEM displacement field. Compared to the moment tensor point source representation the rupture simulation shows differences in waveform, phase and frequency throughout the source region. Additionally, we considered a layered model where we schematized the geology and fault dynamics of the Groningen gas field showing a performance equally well to the homogeneous case. The results show that the approach is successful in coupling a geomechanical model to a wave propagation model, while accurately preserving the rupture mechanism as simulated in the geomechanical model. It has the main advantage that it benefits from efficient run times to calculate surface recordings with the wave propagation model used in the second stage due to a coarser mesh and can be tuned to more complex 3-D geological models given the strong parallel-computing capabilities of SPECFEM. The approach lends itself to compute simulations for a range of combinations of rupture mechanism, reservoir and fault geometry and frictional properties. This in turn can be used to optimize the design of seismic networks such that they are capable of sensing wavefield characteristics containing expressions of fault rupture, from which recorded seismic records can eventually be inverted towards fault rupture mechanism.

REFERENCES

Aki, K. & Richards, P., 2002. *Quantitative Seismology,* 2nd edn, University Science Books, ISBN 0-935702-96-2, 704pp.

Backus, G. & Mulcahy, M., 1976. Moment tensors and other phenomenological descriptions of seismic sources I. Continuous displacements, *Geophys. J. R. astr. Soc.,* **46,** 341–361.

Bao, H., Bielak, J., Ghattas, O., Kallivokas, L.F., O'Hallaron, D.R., Shewchuk, J.R. & Xu, J., 1998. Large-scale simulation of elastic wave propagation in heterogeneous media on parallel computers, *Comput. Methods Appl. Mech. Eng.,* **152**(1), 85–102.

Bielak, J., Loukakis, K., Hisada, Y. & Yoshimura, C., 2003. Domain reduction method for three-dimensional earthquake modeling in localized regions, Part 1: theory, *Bull. seism. Soc. Am.,* **93**(2), 817–824.

Buijze, L., Bogert, P.A.J., Wassing, B.B.T. & Orlic, B., 2019. Nucleation and arrest of dynamic rupture induced by reservoir depletion, *J. geophys. Res.,* **124,** 3620–3645, doi:10.1029/2018JB016941.

Buijze, L., Van Den Bogert, P.A.J., Wassing, B.B.T., Orlic, B. & Ten Veen, J., 2017. Fault reactivation mechanisms and dynamic rupture modelling of depletion-induced seismic events in a Rotliegend gas reservoir, *Neth. J. Geosci.,* **96**(5), 131–148.

Cappa, F. & Rutqvist, J., 2012. Seismic rupture and ground accelerations induced by CO_2 injection in the shallow crust, *Geophys. J. Int.,* **190**(3), 1784–1789.

Cohen, G., 2002. *Higher-Order Numerical Methods for Transient Wave Equations,* Springer.

Fjaer, E., 1999. *Static and Dynamic Moduli of Weak Sandstones,* Rock Mechanics for Industry, pp. 675–681.

Fjaer, E., Holt, R.M., Horsrud, P., Raaen, A.M. & Risnes, R., 1992. *Petroleum Related Rock Mechanics,* Elsevier.

Itasca, 2013. *FLAC3D Fast Lagrangian Analysis of Continua in 3 Dimensions User's Guide,* Itasca Consulting Group.

Kaneko, Y., Ampuero, J.-P. & Lapusta, N., 2011. Spectral-element simulations of long-term fault slip: effect of low-rigidity layers on earthquake-cycle dynamics, *J. geophys. Res.,* **116,** B10313, doi:10.1029/2011JB08395.

Kelly, K.R., Ward, R.W., Treitel, S. & Alford, R.M., 1976. Synthetic seismograms: a finite-difference approach, *Geophysics,* **41,** 2–27.

Klin, P., Priolo, E. & Seriani, G., 2010. Numerical simulation of seismic wave propagation in realistic 3-D geo-models with a Fourierpseudo-spectral method, *Geophys. J. Int.,* **183,** 905–922.

Komatitsch, D., 2011. Fluid-solid coupling on a cluster of GPU graphics cards for seismic wave propagation, *C. R. Acad. Sci., Ser. IIb Mec.,* **339,** 125–135.

Komatitsch, D., Labarta, J. & Michéa, D., 2008. A simulation of seismic wave propagation at high resolution in the inner core of the Earth on 2166 processors of MareNostrum, in *High Performance Computing for Computational Science - VECPAR 2008. VECPAR 2008. Lecture Notes in Computer Science,* Vol. **5336,** Palma, J.M.L.M., Amestoy, P.R., Daydé, M., Mattoso, M. & Lopes, J.C., eds, Springer.

Komatitsch, D. & Tromp, J., 1999. Introduction to the spectral-element method for 3-D seismic wave propagation, *Geophys. J. Int.,* **139**(3), 806–822.

Kosloff, D.D. & Baysal, E., 1982. Forward modeling by a Fourier method, *Geophysics,* **47**(10), 1402–1412.

Ledbetter, H., 1993. Dynamic vs. static Young's moduli: a case study, *Mater. Sci. Eng.: A,* **165**(1), L9–L10.

Levander, A.R., 1988. Fourth-order finite-difference P-SV seismograms, *Geophysics,* **53**(11), 1425–1436.

Maday, Y. & Patera, A.T., 1989. Spectral-element methods for the incompressible Navier-Stokes equations, in *State of the Art Survey in Computational Mechanics,* pp. 71–143, eds Noor, A.K. & Oden, J.T., American Society of Mechanical Engineers.

Mulders, F.M.M., 2003, Modelling of stress development and fault slip in and around a producing gas reservoir, *PhD thesis.* Technical University of Delft (Delft).

Nagelhout, A.C.G. & Roest, J.P.A., 1997. Investigating fault slip in a model of an underground gas storage facility, *Int. J. Rock Mech. Min. Sci.* **34**(3-4), 212.e1–212.e14.

Ohnaka, M., 2013. *The Physics of Rock Failure and Earthquakes.* Cambridge Univ. Press.

Orlic, B. & Wassing, B.B.T., 2013. A study of stress change and fault slip in producing gas reservoirs overlain by elastic and viscoelastic caprocks, *Rock Mech. Rock Eng.* **46**(3), 421–435.

Paap, B., Kraaijpoel, D., Bakker, M. & Gharti, H.N., 2018. Wave propagation modelling of induced earthquakes at the Groningen gas production site, *Geophys. J. Int.,* **214,** 1947–1960.

Patera, A.T., 1984. A spectral element method for fluid dynamics: laminar flow in a channel expansion, *J. Comp. Phys.,* **54,** 468–488.

Rutqvist, J., 2011. Status of the TOUGH-FLAC simulator and recent applications related to coupled fluid flow and crustal deformations, *Computers & Geosciences,* **37**(6), 739–750.

Seriani, G. & Oliveira, S., 2008. Dispersion analysis of spectral element methods for elastic wave propagation, *Wave Motion,* **45,** 729–744.

SPECFEM2D User Manual, 2015. Princeton University (USA) and CNRS / University of Marseille, Version 7.0.

Tromp, J., Komatitsch, D. & Liu, Q., 2008. Spectral-element and adjoint methods in seismology, *Commun. Comput. Phys.,* **3**(1), 1–32.

Tsuboi, S., Ando, K., Miyoshi, T., Peter, D., Komatitsch, D. & Tromp, J., 2016, A 1.8 trillion degrees-of-freedom, 1.24 petaflops global seismic wave simulation on the K computer, *Int. J. High Perf. Comp. Appl.,* **30,** doi:10.1177/1094342016632596.

Uenishi, K. & Rice, J.R., 2003. Universal nucleation length for slip-weakening rupture instability under nonuniform fault loading, *J. geophys. Res.,* **108,** 2042, doi:10.1029/2001JB001681, B1.

van Thienen-Visser, K. & Breunese, J., 2015. Induced seismicity of the Groningen gas field: History and recent developments, *Leading Edge,* **34**(6), 664–671.

van Wees, J., Osinga, S., Van Thienen-Visser, K. & Fokker, P., 2018. Reservoir creep and induced seismicity: inferences from geomechanical modeling of gas depletion in the Groningen field, *Geophys. J. Int.,* **212**(3), 1487–1497.

Verweij, H., Simmelink, H., Underschultz, J. & Witmans, N., 2012. Pressure and fluid dynamic characterisation of the Dutch subsurface, *Neth. J. Geosci.,* **91**(4), 465–490.

Wang, X. & Cai, M., 2016. FLAC/SPECFEM2D coupled numerical simulation of wavefields near excavation boundaries in underground mines, *Comp. Geosci.,* **96,** 147–158.

Wassing, B.B.T., Buijze, L. & Orlic, B., 2016. *Modelling of Fault Reactivation and Fault Slip in Producing Gas Fields using a Slip-Weakening Law,* American Rock Mechanics Association, 16-658, Proceedings.

Wassing, B.B.T., Buijze, L., Orlic, B. & Osinga, S., 2017. *The Impact of Viscoelastic Caprock on Fault Reactivation and Fault Rupture in Producing Gas Field,* American Rock Mechanics Association, 17-355, Proceedings.

B.T.Wassing, B., van Wees, J.-D. & Fokker, P.A., 2014. Coupled continuum modeling of fracture reactivation and induced seismicity during enhanced geothermal operations, *Geothermics,* **52,** 153–164.

Zbinden, D., Rinaldi, A.P., Urpi, L. & Wiemer, S., 2017. On the physics-based processes behind production-induced seismicity in natural gas fields, *J. geophys. Res.,* **22**(5), 3792–3812.

Zienkiewicz, O.C. & Taylor, R.L., 2000. *The Finite Element Method,* Butterworth Heinemann.

Zoback, M.D., 2007. *Reservoir Geomechanics.* Cambridge Univ. Press.

APPENDIX: NOTE ON SEISMIC VELOCITIES

Seismic *P*- and *S*-wave velocities (respectively V_p and V_s) were calculated from the known bulk and shear moduli. When using these relations, one should consider the difference between the static and dynamic moduli. Static moduli are determined with deformation experiments in a laboratory on dry rock samples, whereas dynamic moduli are calculated from elastic wave velocities and densities and based on undrained rock. The static and dynamic moduli are equal for homogeneous, elastic materials (Ledbetter 1993). Differences between static and dynamic moduli are caused by heterogeneity of the microstructure of rocks, originating at grain contacts, since stress concentrations in contact areas may exceed elastic limits at low external stresses (Fjaer *et al.* 1992). These differences are expressed in strain amplitude. Static moduli are measured as slopes of stress–strain curves and differ from small strain amplitude dynamic (elastic) moduli because of plasticity or non-linear effects (Fjaer *et al.* 1992; Zoback 2007). Fjaer (1999) determined a relation between static and dynamic moduli specifically for weak sandstones. Establishing similar relationships for lithologies considered in our model requires additional laboratory measurements and is beyond the scope of this research. Here, we neglect the relations between static and dynamic moduli, but simply use dynamic moduli in the geomechanical model that are representative of the seismic velocities. Although this results in an overestimation of the elastic moduli within the geomechanical model, this will not affect the demonstration of our combined coupling approach.